An anisotropic vector hysteresis model of ferromagnetic behavior under alternating and rotational magnetic field

Benjamin Ducharne, S. Zurek, Laurent Daniel, Gaël Sebald

An anisotropic vector hysteresis model of ferromagnetic behavior under alternating and rotational magnetic field

B. Ducharne[1,2], S. Zurek[3], L. Daniel[4,5], G. Sebald[2]

[1] LGEF, INSA Lyon, Villeurbanne, France.

[2] ELyTMaX UMI 3757, CNRS – Université de Lyon – Tohoku University, International Joint Unit, Tohoku University, Sendai, Japan.

[3] Megger Instruments, Archcliffe Road, Dover, CT17 9EN, United Kingdom

[4] Université Paris-Saclay, Centrale Supélec, CNRS, Group of Electrical Engineering-Paris (GeePs), 91192, Gif-sur-Yvette, France.

[5] Sorbonne Université, CNRS, Group of Electrical Engineering-Paris (GeePs), 75252, Paris, France.

Abstract :

Vector quantities and tensorial properties rule the magnetization mechanisms in ferromagnetic materials. Every ferromagnetic material is anisotropic to some degree in its magnetic response, so this anisotropy has to be considered for a general model. In this study, a multiscale approach based on a statistical description of the magnetic domain distribution and the knowledge of the crystallographic texture is used to predict the anhysteretic behavior along an arbitrary space direction. Combined with the vector Bergqvist dry-friction hysteresis model, qualitatively reliable simulation results are obtained under alternating and rotational magnetization. FeSi 3% grain-oriented (FeSi GO) electrical steel is chosen as study material: FeSi GO are widespread so that extensive data are available and strongly anisotropic, forcing the model toward the “worst-case” scenario from the viewpoint of anisotropy.

Moreover, under high excitation of rotational magnetization, losses drop due to the disappearance of the magnetic domains. This behavior is represented correctly by the proposed simulation method. In such conditions, the magnetization behavior is led mainly by the anhysteretic behavior, strengthening the predictive ability of the proposed model. In this manuscript, comparisons between simulations and measurements under many amplitudes of alternating and rotational magnetization for different levels of imposed excitation or magnetization are provided and used to validate the simulation method.

Keywords : multiscale model, dry friction model, hysteresis losses

1 – Introduction

It is established that almost 3% of the electricity is lost in the magnetic cores [1]. In many applications (such as transformers), magnetization directions are well established and remain unchanged under operation. Alternating losses are then preponderant. For such applications, highly anisotropic ferromagnetic materials are industrially most suitable [2]. They favor magnetization in privileged directions and improve the conversion efficiency.

In many other applications (such as motors), it is more favorable to avoid highly anisotropic magnetic cores [3]. In most of the geometry, the magnetization direction varies over time. Alternating losses are still present, but the amount of rotational loss increases significantly (up to 50 % [1]).

The prediction of the magnetic core behavior is an essential task in the design of electromagnetic devices. Constitutive analytical equations [4][5] and simulation methods [6]-[9] have been proposed, but progress is still to be made in this strongly nonlinear and vector environment.

Anisotropy in laminated electrical steel sheets is of genuine interest as witnessed by the vast list of article dealing with this topic [10]-[17].

According to [18], ferromagnetic vector hysteresis models can be classified into two categories:

- “type I” is built from the superposition of scalar models continuously distributed along all possible directions.
- “type II” solves the hysteresis problem by integrating contributions of intrinsically vector elements.

The classical Preisach model has already been modified to become a “type I” [19][20] or a “type II” [21] vector model. In [22], d’Aquino et al. proposed a “type I” Preisach vector model. This phenomenological approach is interesting but limited to isotropic materials. It is inadequate to simulate the strongly anisotropic FeSi GO laminations. This simulation method is descriptive (as opposed to predictive) as the experimental data used to validate and set the simulation parameters are the same. The model is then limited to pre-defined experimental conditions. Excellent fits are observed when those conditions are provided.

The also classical Jiles-Atherton model (JA) has as well already been converted to a “type II” to generate vector results [23]-[25].

All these examples follow the general trend observed in [18]: “the extrapolation of solidly established scalar unidirectional models to the case where the field rotates in the lamination plane”. All these simulation methods can be set precisely and provide accurate simulation results, but drawbacks remain, and the physical interpretations are limited.

In 1996, Bergqvist [26] proposed a “type II” vector hysteresis model based on pseudo particles. It introduces an ideal soft ferromagnetic material without hysteresis, which is ruled by a single-valued magnetization curve called anhysteretic curve and expressed as $\mathbf{M} = \mathbf{M}_{\mathrm{anh}}(\mathbf{H}_{\mathrm{surf}})$. $\mathbf{M}$ is the magnetization, $\mathbf{M}_{\mathrm{anh}}$ the anhysteretic magnetization, and $\mathbf{H}_{\mathrm{surf}}$ the tangential surface excitation field. Then, inside the real ferromagnetic material, he suggested the presence of potential wells generating sequences of small discontinuous jumps similar to dry frictions. If their number approaches infinity, the magnetic behavior results in a well-defined hysteresis shape. Bergqvist Dry Friction (B-DF) model is convenient as it relies on physical fundaments and behaves correctly

under alternating and rotating magnetization. It furthermore reproduces some of the rotational losses peculiar behaviors, including the loss drop at high inductions.

In this study, we specifically focus on the anisotropy question. For this, the B-DF model will be combined with a multiscale model developed to predict anhysteretic behaviors [27]. Grain-oriented electrical steel specimens (GO FeSi 3%) are chosen due to their highly anisotropic magnetic properties.

2 – Anisotropic vector hysteresis model

2.1 The dry friction vector hysteresis model (B-DF)

In physics, analogies are commonly used as indirect ways to understand and simulate phenomena impossible to observe in the first place [28]. Hysteretic behavior of mechanical friction force has been observed and discussed for years [29]-[32]. The analogy with ferromagnetic hysteresis is evident, and it has already served to develop accurate simulation tools [33][34]. The B-DF model, as described by Bergqvist in [26], is one of them. This model relies on energetical principles. More precisely, it is based on multiple discretized dry-friction elements. Each element is characterized by its threshold κ and weight Spectrum(κ). A dry-friction element is ruled by sequence (1):

$$\begin{aligned}
&\text{if } |\mathbf{H}_{\mathbf{surf}}(\mathrm{t}) - f^{-1}(\mathbf{M}(\mathrm{t}-\mathrm{dt}))| > \kappa \\
&\mathbf{v} = \frac{\mathbf{H}_{\mathrm{surf}}(\mathrm{t}) - f^{-1}(\mathbf{M}(\mathrm{t}-\mathrm{dt}))}{|\mathbf{H}_{\mathrm{surf}}(\mathrm{t}) - f^{-1}(\mathbf{M}(\mathrm{t}-\mathrm{dt}))|} \\
&\kappa = |\mathbf{H}_{\mathrm{surf}}(\mathrm{t}) - f^{-1}(\mathbf{M}(\mathrm{t}-\mathrm{dt})) - \mathrm{A}\mathbf{v}| \\
&\mathbf{M}(\mathrm{t}) = f(f^{-1}(\mathbf{M}(\mathrm{t}-\mathrm{dt})) + \mathrm{A}\mathbf{v}) \\
&\text{else } \mathbf{M}(\mathrm{t}) = \mathbf{M}(\mathrm{t}-\mathrm{dt})
\end{aligned} \tag{1}$$

Where A is a constant, and $\mathbf{v}$ is a unit vector giving the direction of change [26]. Their values are calculated at each simulation step time.

In [18], $\eta = f^{-1}(\mathbf{M}(\text{t-dt}))+A\mathbf{v}$ is introduced as a rest field and is defined as the field that would produce the current magnetization in the absence of hysteresis. f is a sigmoid function related to the anhysteretic behavior, M_s is the saturation magnetization and a a constant:

$$\mathbf{M}_{\text{anh}} = M_s \cdot \tanh(a \cdot \mathbf{H}_{\text{surf}}) \quad (2)$$

Under unidirectional excitation ($\mathbf{M}$ and $\mathbf{H}_{\text{surf}}$ supposed colinear), high amplitude and symmetrical $\mathbf{H}_{\text{surf}}$, the resolution of sequence (1) leads to a well-shaped major hysteresis cycle. Unfortunately, sequence (1) is unable to simulate the first magnetization curve (Fig. 1 – a) correctly. This issue is solved once the distribution of dry elements is taken into account. In [35], the spectrum function is introduced to condense all the dry-friction element weights:

$$\sum_{i=1}^{q} \text{Spectrum}(\kappa_i)\mathbf{M}_i = \mathbf{M} \quad (3)$$

This Gaussian-like distribution can be obtained numerically [36] or expressed analytically as follows:

$$\text{Spectrum}(\kappa_i) = \frac{e^{-\frac{(\kappa_i-\mu_d)^2}{2\theta_d^2}}}{\theta_d\sqrt{2\pi}} \quad (4)$$

The number of dry-friction elements is not limited. Eq. (5) gives the unique condition to be fulfilled for coherent values on the induction axis.

$$\sum_{i=1}^{q} \text{Spectrum}(\kappa_i) = 1 \quad (5)$$

Fig . 1 – b shows a unidirectional $\mathbf{B}_a(\mathbf{H}_{\text{surf}})$ first magnetization and major hysteresis loop simulated with the B-DF model for a typical GO FeSi. Where $\mathbf{B}_a$ is the average cross-section induction calculated from Eq. (6):

$$\mathbf{B}_a = \mu_0(\mathbf{H}_{surf} + \mathbf{M}) \tag{6}$$

The anhysteretic contribution is obtained with the analytical expression Eq. (2). Tab. 1 gives the simulation parameters, and the Spectrum function is depicted in Fig. 2 – c. The B-DF model parameters are set following two steps:

- An optimization window is established for both parameters (μ_d, θ_d). The product of μ_d and $\Delta\kappa$ is close to the resulting unidirectional coercivity in the $\mathbf{B}_a(\mathbf{H}_{surf})$ hysteresis loop. Similarly, θ_d is close to the ratio between the differential permeability read on the anhysteretic curve $\mathbf{B}_{anh}(\mathbf{H}_{surf})$ at $\mathbf{H}_{surf}$ =0 and read at the coercivity of the unidirectional $\mathbf{B}_a(\mathbf{H}_{surf})$ hysteresis curve.
- The minimization of the mean relative standard deviation error function:

$$\text{Err}\,(\%) = \frac{100}{n}\sum_{i=1}^{n}\frac{\left|\mathbf{B}_{a_{i_{meas}}}(\mathbf{H}_{surf_i}) - \mathbf{B}_{a_{i_{sim}}}(\mathbf{H}_{surf_i})\right|}{\mathbf{B}_{a_{i_{meas}}}(\mathbf{H}_{surf_i})} \tag{7}$$

Where n represents the discrete data points obtained experimentally. In the specific case of Fig. 1, q = 200 dry elements were considered, $\Delta\kappa = 1$.

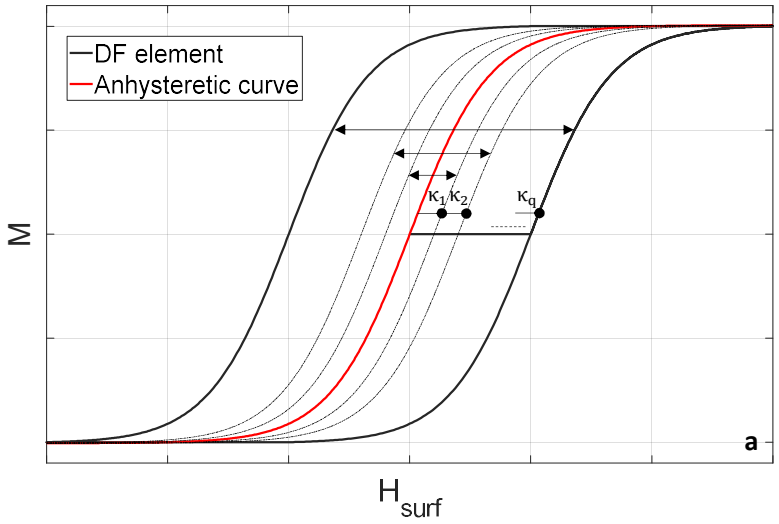

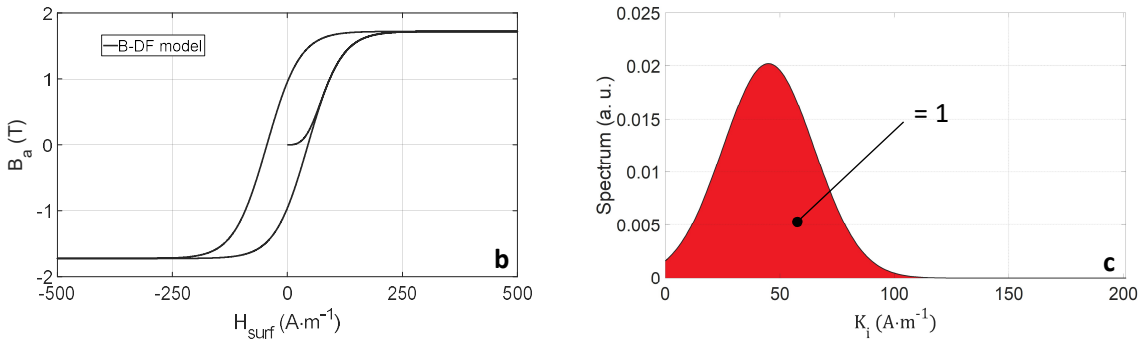

Fig. 1 – a Major hysteresis cycle and first magnetization curve as obtained by solving sequence (1). Fig. 1 – b B-DF, first magnetization curve, and major hysteresis loop for a typical FeSi 3% GO laminated electrical steel sheet (rolling direction). Fig. 1 – c Spectrum distribution for q = 200.

Tab. 1 – Fig. 1 – b B-DF simulation parameters.

B-DF Parameters	Typical value
a (m·A^{-1})	1.5 10^{-2}
M_s (A·m^{-1})	1.37 10^{6}
μ_d	45
θ_d	20
q	200

The B-DF model in its original form is frequency-independent. Thus its viability under rotational magnetization can only be observed by plotting the $\mathbf{B}_a$ dependence of the rotational losses W_{rot} under very-low-frequency circular magnetization, below the quasi-static threshold (Eq. (8))(Fig. 2).

$$W_{rot} = \int_0^T \left(\frac{dB_{ax}(t)}{dt} H_{surfx}(t) + \frac{dB_{ay}(t)}{dt} H_{surfy}(t) \right) dt \quad (8)$$

Where B_{ax}, B_{ay}, $H_{surfx,}$ and H_{surfy}, are the x and y-axis projections of $\mathbf{B}_a$ and $\mathbf{H}_{surf,}$ respectively, and T is the magnetization period.

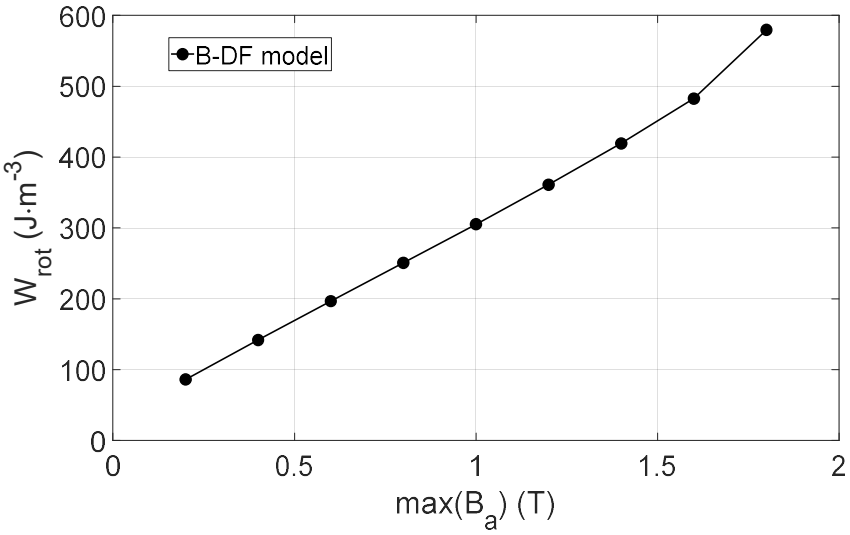

Fig. 2 Magnetic losses under rotational magnetization as a function of the maximal magnetic field amplitude, as simulated with sequence (1).

Fig. 2 shows a correct trajectory in the low induction range. However, it incorrectly keeps increasing even beyond the "saturation elbow" (≈ 1.5 T for this material). In practice, the quasi-static rotational losses decline in the high induction regime following the disappearance of the magnetic domains [37]. The simulation method described above is therefore unable to reproduce this drop. This issue was solved in [26] by conserving the Spectrum function but replacing the constant $\Delta\kappa_i$ step between every element coercivities with a rest field-dependent distribution function:

$$\Delta\kappa_i = \frac{\Delta\kappa_{i_0}}{\left(1+\left(\frac{|\eta|}{k_d}\right)^2\right)} \tag{9}$$

Here k_d is an additional parameter set to optimize the simulation/measurement comparisons. As the alternating losses are relatively independent of k_d (Fig. 3 – b), the optimization process for a precise estimation of this parameter relies on W_{rot}. Fig. 3 – a shows the $\mathbf{B}_a$ dependence of W_{rot} for the updated simulation method and increasing values of k_d. Fig. 3 – b shows the $\mathbf{B}_a$

dependence of W_{alt} for the same simulation parameters. Eventually, Fig. 3 – c depicts the simulated unidirectional hysteresis cycles as obtained with and without the correction (k_d = 80) and confirms the low influence of k_d in a unidirectional situation.

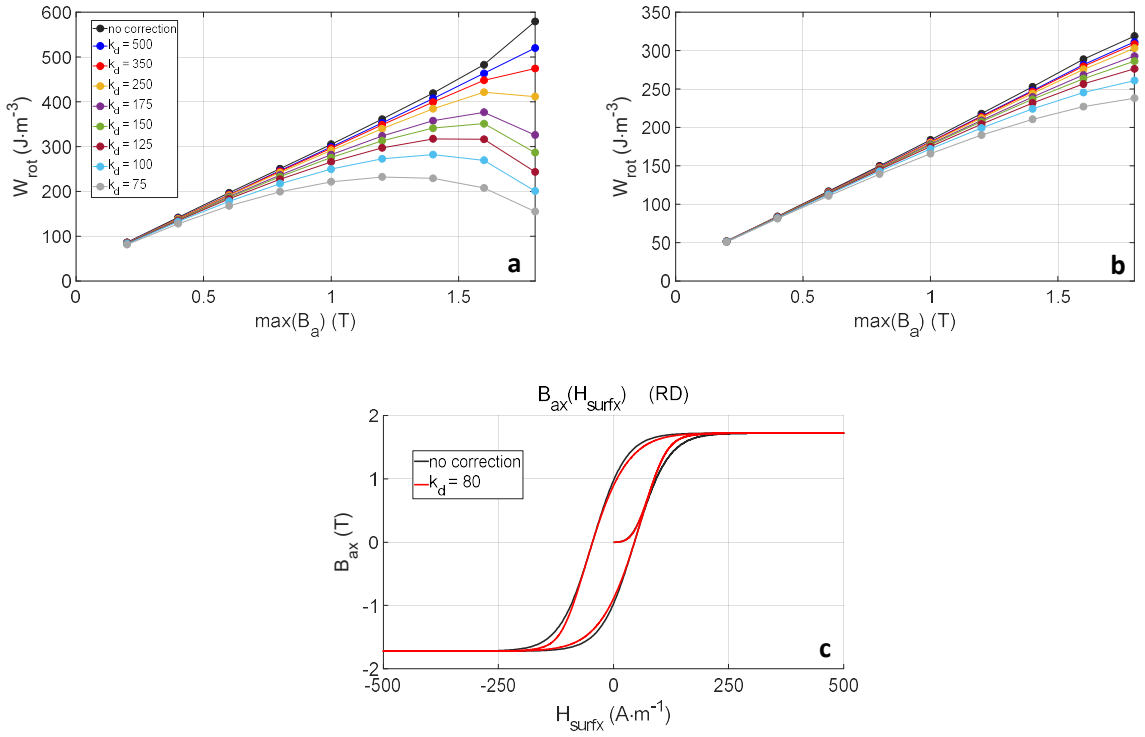

Fig. 3 – a W_{rot} as a function of max($\mathbf{B}_a$) without the correction and for different values of k_d. Fig. 3 – b W_{alt} as a function of max($\mathbf{B}_a$) in the same conditions. Fig. 3 – c Comparison on the unidirectional hysteresis cycle with and without the correction (k_d = 80).

2.2 Anhysteretic behavior: the MultiScale Model MSM

MSM [38][39] has been developed to predict the anhysteretic magnetic behavior of a ferromagnetic specimen. It relies on a statistical description of the distribution of the ferromagnetic domains. MSM provides vector information, and the anisotropy effects are naturally taken into account [27]. A polycrystalline ferromagnetic specimen is considered as an aggregate of single crystals (grains). Each grain is supposed to be divided into a finite number of

magnetic domain families. A little less than 3.5 10^4 families for each grain orientation have been considered for the FeSi GO tested in this study. Each domain family is characterized by its own magnetic orientation α and its own potential energy W_α (Eq. 10) where W_α^k, W_α^H, W_α^σ, and W_α^{conf} stand for the magneto-crystalline (Eq. (11)), magnetostatic (Eq. (12)), magneto-elastic (Eq. (13)), and initial configuration energy, respectively:

$$W_\alpha = W_\alpha^K + W_\alpha^H + W_\alpha^\sigma + W_\alpha^{conf} \tag{10}$$

$$W_\alpha^K = K_1(\gamma_1^2\gamma_2^2 + \gamma_2^2\gamma_3^2 + \gamma_3^2\gamma_1^2) + K_2\,\gamma_1^2\gamma_2^2\gamma_3^2 \tag{11}$$

$$W_\alpha^H = -\mu_0 \mathbf{H}_\alpha . \mathbf{M}_\alpha \tag{12}$$

$$W_\alpha^\sigma = -\boldsymbol{\sigma}_\alpha : \boldsymbol{\varepsilon}_\alpha^\mu \tag{13}$$

$\mathbf{H}_\alpha$, $\mathbf{M}_\alpha$, $\boldsymbol{\sigma}_\alpha$ and $\boldsymbol{\varepsilon}_\alpha^\mu$ are the magnetic field, the magnetization, the stress tensor, and the magnetostriction strain tensor defined at the magnetic domain scale, respectively. The inital configuration energy W_α^{conf} is used to account for a potential misbalance in the initial domain configuration of the material in the absence of external magnetic field or mechanical stress. In GO steels, this initial misbalance can be interpreted as the result of a free-surface effect [27]. It was later shown [39] that initial configuration effects can be treated as the result of a fictitious initial stress $\boldsymbol{\sigma_0}$ in the material, this fictitious homogeneous mechanical stress being interpreted as the image of the initial configuration source (be it internal stress, plasticity, surface or geometrical effects, ...). The expression of W_α^{conf} is then similar to Eq. (13), with $\boldsymbol{\sigma_0}$ instead of $\boldsymbol{\sigma}_\alpha$. In the following $\boldsymbol{\sigma_0}$ will be taken as a uniaxial stress of amplitude σ_0 along RD. $\mathbf{M}_\alpha$ is defined by its norm (the material saturation magnetization M_s), and its direction is given by γ_1, γ_2, γ_3. $\boldsymbol{\varepsilon}_\alpha^\mu$ is defined by the magnetostriction constants λ_{100} and λ_{111} [27]. K_1 and K_2 are the magneto-crystalline energy constants.

The volume fraction f_α of a domain family is calculated from the knowledge of the potential energy of all domain families:

$$f_\alpha = \frac{\exp\left(-A_S \, \mathrm{W}_\alpha\right)}{\sum_\alpha \exp\left(-A_S \, \mathrm{W}_\alpha\right)} \tag{14}$$

A_S is a material parameter that can be adjusted using the initial macroscopic susceptibility χ^0 of the unstressed anhysteretic magnetization curve [38].

Once f_α is calculated for all magnetic domains families, the magneto-elastic response at the grain scale is calculated by a volume average:

$$\boldsymbol{\varepsilon}_{\mathrm{g}}^{\mu} = \langle \boldsymbol{\varepsilon}_{\alpha}^{\mu} \rangle = \sum_\alpha f_\alpha \, \boldsymbol{\varepsilon}_{\alpha}^{\mu} \tag{15}$$

$$\mathbf{M}_{\mathrm{g}} = \langle \mathbf{M}_\alpha \rangle = \sum_\alpha f_\alpha \, \mathbf{M}_\alpha \tag{16}$$

An orientation distribution function (crystallographic orientations) obtained from X-ray diffraction or Electron Back Scattering Diffraction (EBSD) measurements can be used to describe the crystallographic texture and return the behavior at the polycrystalline scale.

For simplification reasons, both magnetic $\mathbf{H}$ and mechanical $\boldsymbol{\sigma}$ external stimuli are supposed uniform within the material. The potential energy and the volume fraction of each magnetic domain family calculus come first. It is followed by each grain magnetization (Eq. (16)). Eventually, an average over the whole volume is performed to obtain the entire specimen magnetization:

$$\mathbf{M} = \langle \mathbf{M}_{\mathrm{g}} \rangle \tag{18}$$

This process allows constructing the stress-dependent anhysteretic magnetization curves based on a limited number of intrinsic material parameters. The magnetic induction is finally easily deduced from the magnetization using Eq. (6).

In this study, the simulation parameters and the crystallographic texture data for a typical GO FeSi come from [27] (Hi-B, 0.3 mm thick from Nippon Steel), except σ_0 (not used in ref [27]). It is worth mentioning that M_s has been slightly reduced to improve the comparisons with the experimental results. The texture of oriented grain electrical steel specimens being especially strong, accurate simulation results can be obtained with an orientation distribution function limited to 60 orientations. The simulation parameters are summarized in Tab. 2 below:

Tab. 2 – MSM simulation parameters for the GO FeSi.

Quantity **Unit**	M_s A·m^{-1}	K_1 ; K_2 kJ·m^{-3}	λ_{100} ; λ_{111} -	A_S m^3·J^{-1}	σ_0 MPa
For FeSi GO	1.37·10^6	38 ; 0	23·10^{-6} ; -4.5·10^{-6}	2·10^{-2}	7

Fig. 4 – a shows simulated anhysteretic curves for the GO FeSi along different orientations in the lamination plane. θ = 0° is the rolling direction (RD - easy axis), θ = 90° is the transverse direction (TD). Fig. 4 – b gives the resulting induction levels for a given H_{surf} as a function of θ. The significant differences between RD and TD are noteworthy, and an especially unfavorable direction is observed at approximately 55° (usual observation for GO electrical steel [40]-[44]).

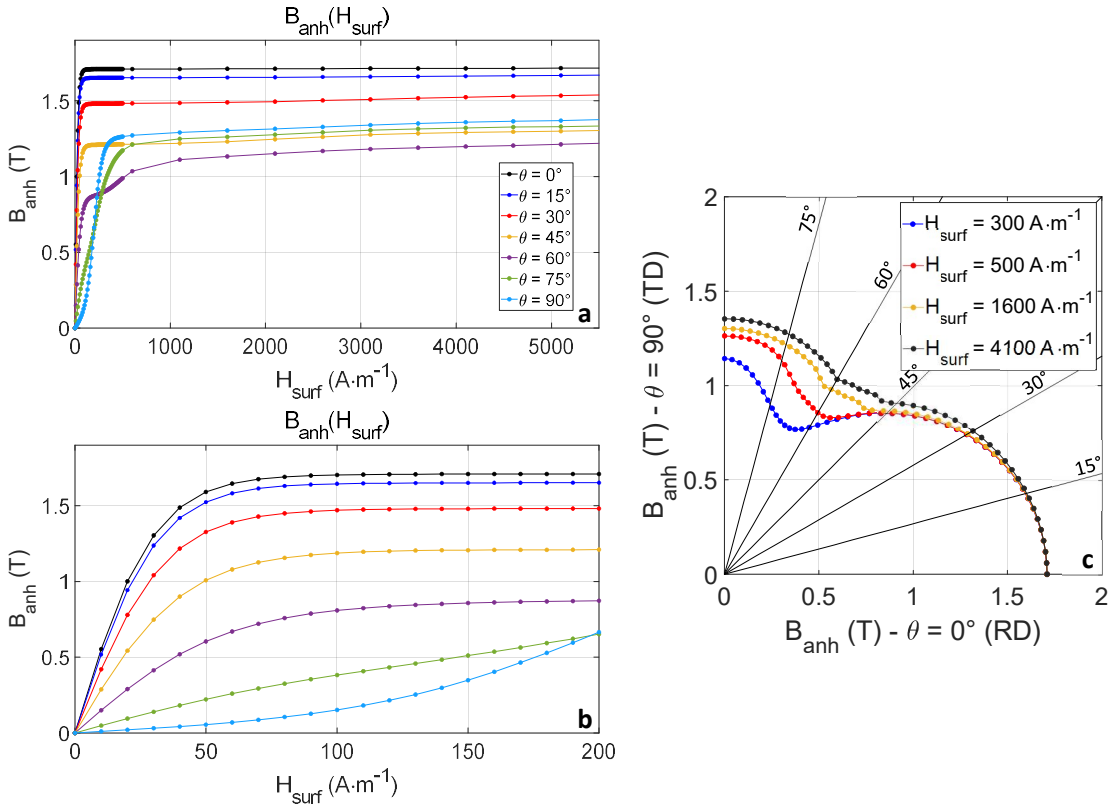

Fig. 4 – a Simulated anhysteretic curves for different orientations in the lamination plane. Fig. 4 – b Same plot at a different x-axis scale. Fig. 4 – c Induction level for a given $\mathbf{H}_{surf}$ as a function of θ.

2.3 Integration of the multiscale model in the B-DF model

The B-DF model in its quasi-static and original form [26], as described in section 2.1 relies on five parameters. The resolution of the accommodation and congruency issues by considering an effective field as input of the model is not discussed in this manuscript. Still, it is giving rise to a sixth parameter, α:

$$\mathbf{H}_e = \mathbf{H}_{surf} + \alpha \cdot \mathbf{B}_a \tag{19}$$

Among these five parameters, M_s and a are known as the anhysteretic ones. Together in Eq. (2), they control the anhysteretic behavior. M_s is a material constant. For isotropic materials, a can also be set constant, independently from the magnetization azimuthal angle φ and polar angle θ. Oppositely, for anisotropic materials, accurate simulations results can only go through a

φ and θ dependency of $a(\varphi, \theta)$. Also, to consider the amplitude variation (Fig. 4 – a), a new parameter is defined: $\mathbf{M}$ at $\mathbf{H}_{surf}$ = 5 kA·m^{-1} also dependent on φ and θ: $M_{5000}(\varphi, \theta)$.

MSM provides anhysteretic curves in every space direction and orientation. The simulated anhysteretic curves come as data files, and a preliminary stage consists of converting these data into analytical expressions (sigmoid function, Eq. (2)). In this study, all the experimental results were measured in the lamination plane (i.e., φ = 0). Thus, the simulation results were limited to this condition. Due to their fabrication process, the studied materials are orthotropic, so that θ can also be restricted to $[0 - 90]°$ [45].

As revealed clearly in [27][43], the magnetization curve of the GO FeSi laminations show a staircase shape in the TD. This staircase shape mostly affects the material response at low fields. The use of the initial configuration energy W_α^{conf} allows this effect to be modeled by the MSM.

In order to improve the quality of the analytical fits (including the staircase shape), the sigmoid function (Eq. (2)) has been slightly modified and enriched with two parameters, $\tau(\theta)$, $b(\theta)$:

$$\mathbf{M}_{anh} = M_{5000}(\theta) \cdot \tanh\left(a(\theta) \cdot \mathbf{H}_{surf} \cdot \left(1 - e^{-\frac{\mathbf{H}_{surf}}{\tau(\theta)}}\right)\right) + b(\theta) \cdot \mathbf{H}_{surf} \qquad (2.2)$$

Once the θ dependence of M_{5000}, a, τ and b was established (Fig. 5), an analytical expression (harmonic type) of these functions was proposed to facilitate their incorporation in the B-DF model (becoming the MSM-DF model). Matlab® curve fitting toolbox was used to determine these expressions. Fig. 5 displays M_{5000}, a, τ and b as a function of θ as simulated with the multiscale model and the comparison with the analytical expression obtained from the Matlab® curve fitting toolbox. Tab. 3 below gives these analytical expressions.

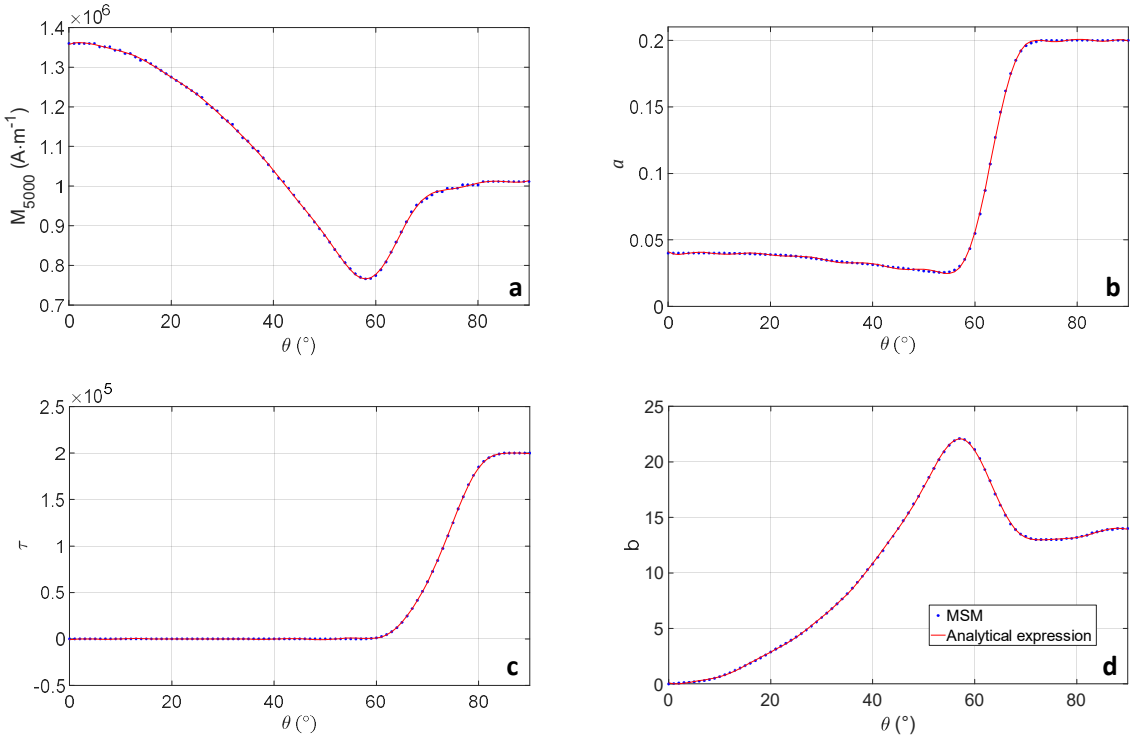

Fig. 5 – a $M_{5000}(\theta)$, comparison multiscale model / analytical expression. Fig. 5 – b $a(\theta)$ comparison multiscale model / analytical expression. Fig. 5 – c $\tau(\theta)$ comparison multiscale model / analytical expression. Fig. 5 – d $b(\theta)$ comparison multiscale model / analytical expression.

Tab. 3 – Analytical expression $M_{5000}(\theta)$, $a(\theta)$, $\tau(\theta)$ and $b(\theta)$.

$$X = \boldsymbol{U_0} + \boldsymbol{U_1}\cos(\theta \cdot \boldsymbol{U_w}) + \boldsymbol{V_1}\sin(\theta \cdot \boldsymbol{U_w}) + \boldsymbol{U_2}\cos(2\theta \cdot \boldsymbol{U_w}) + \boldsymbol{V_2}\sin(2\theta \cdot \boldsymbol{U_w}) + \boldsymbol{U_3}\cos(3\theta \cdot \boldsymbol{U_w}) + \boldsymbol{V_3}\sin(3\theta \cdot \boldsymbol{U_w}) + \boldsymbol{U_4}\cos(4\theta \cdot \boldsymbol{U_w}) + \boldsymbol{V_4}\sin(4\theta \cdot \boldsymbol{U_w}) + \boldsymbol{U_5}\cos(5\theta \cdot \boldsymbol{U_w}) + \boldsymbol{V_5}\sin(5\theta \cdot \boldsymbol{U_w}) + \boldsymbol{U_6}\cos(6\theta \cdot \boldsymbol{U_w}) + \boldsymbol{V_6}\sin(6\theta \cdot \boldsymbol{U_w}) + \boldsymbol{U_7}\cos(7\theta \cdot \boldsymbol{U_w}) + \boldsymbol{V_7}\sin(7\theta \cdot \boldsymbol{U_w}) + \boldsymbol{U_8}\cos(8\theta \cdot \boldsymbol{U_w}) + \boldsymbol{V_8}\sin(8\theta \cdot \boldsymbol{U_w})$$

$\boldsymbol{X}$	M_{5000}	a	τ	b
$\boldsymbol{U_0}$	1091400	0.08838	-3993000	9.969
$\boldsymbol{U_1}$	218705	0.01667	1476000	-7.384
$\boldsymbol{V_1}$	103530	-0.08604	7169000	-3.977
$\boldsymbol{U_2}$	-16303	-0.04337	5158000	0.5014
$\boldsymbol{V_2}$	35147.5	-0.009779	-2223000	-2.314
$\boldsymbol{U_3}$	55913	0.000431	-2053000	-2.556
$\boldsymbol{V_3}$	6845.05	0.002251	-2924000	0.3361
$\boldsymbol{U_4}$	-3564.05	-0.01373	-1264000	0.2652
$\boldsymbol{V_4}$	-15274.5	-0.00811	1352000	0.02128
$\boldsymbol{U_5}$	10625	-0.006512	647400	-0.8497
$\boldsymbol{V_5}$	3157.75	0.00944	390000	0.2104
$\boldsymbol{U_6}$	-1923.55	0.000866	74430	0.2066
$\boldsymbol{V_6}$	-9945	0.000472	-217800	0.3
$\boldsymbol{U_7}$	-142.205	-0.003273	-46550	-0.2141
$\boldsymbol{V_7}$	3842	0.002473	-5407	0.1101
$\boldsymbol{U_8}$	2495.6	0.001683	463.1	0.1473
$\boldsymbol{V_8}$	-2805	0.002382	4843	0.1862
$\boldsymbol{U_w}$	0.048416	0.06024	0.03117	0.05497

Alternating excitation predictions are given in Fig. 6 and 7. The staircase shape is visible when θ is getting closer to 90°.

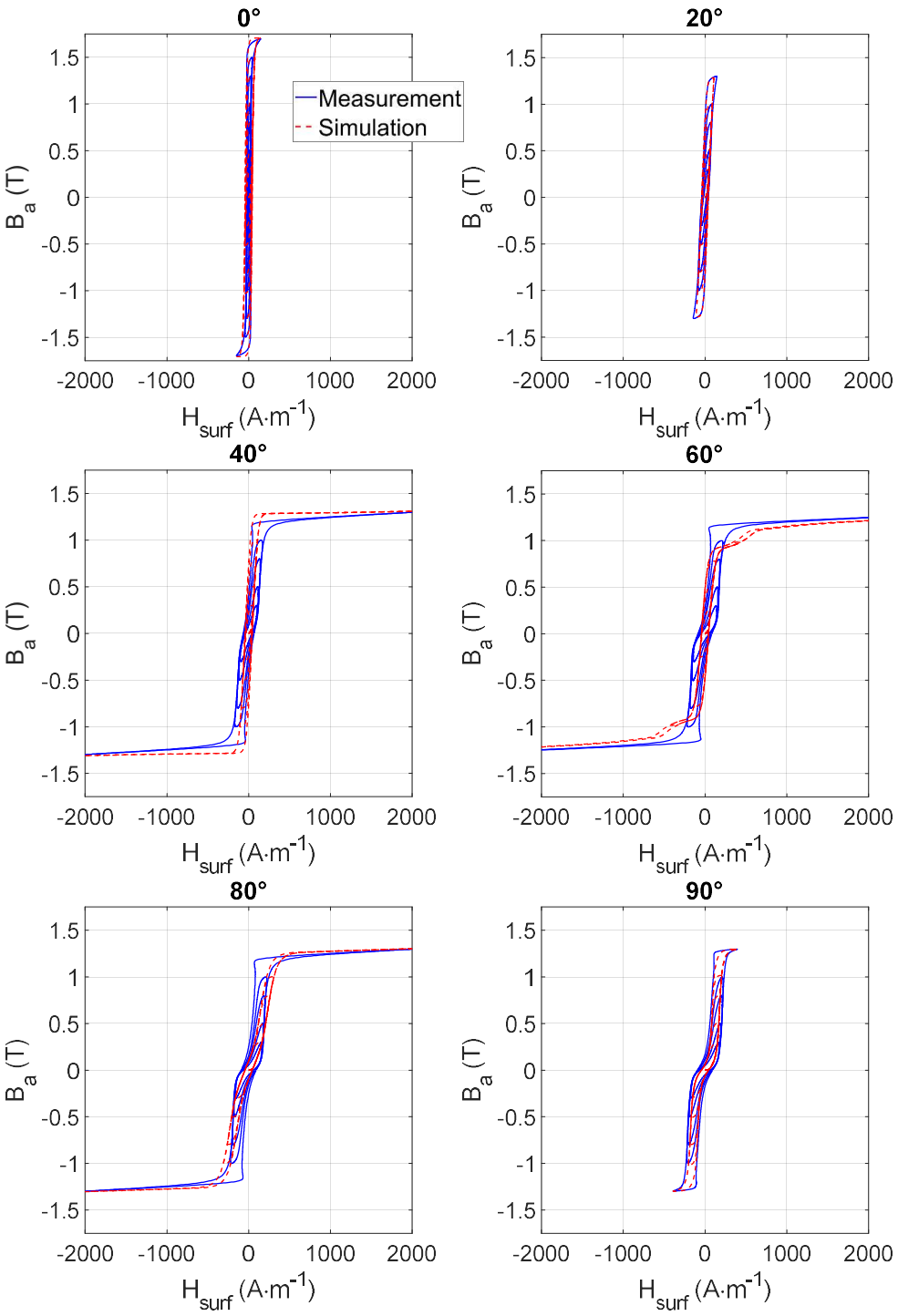

Fig. 6 Comparison simulation/measurement for quasi-static minor centered cycles under unidirectional alternating conditions and six different angles (same axis scale).

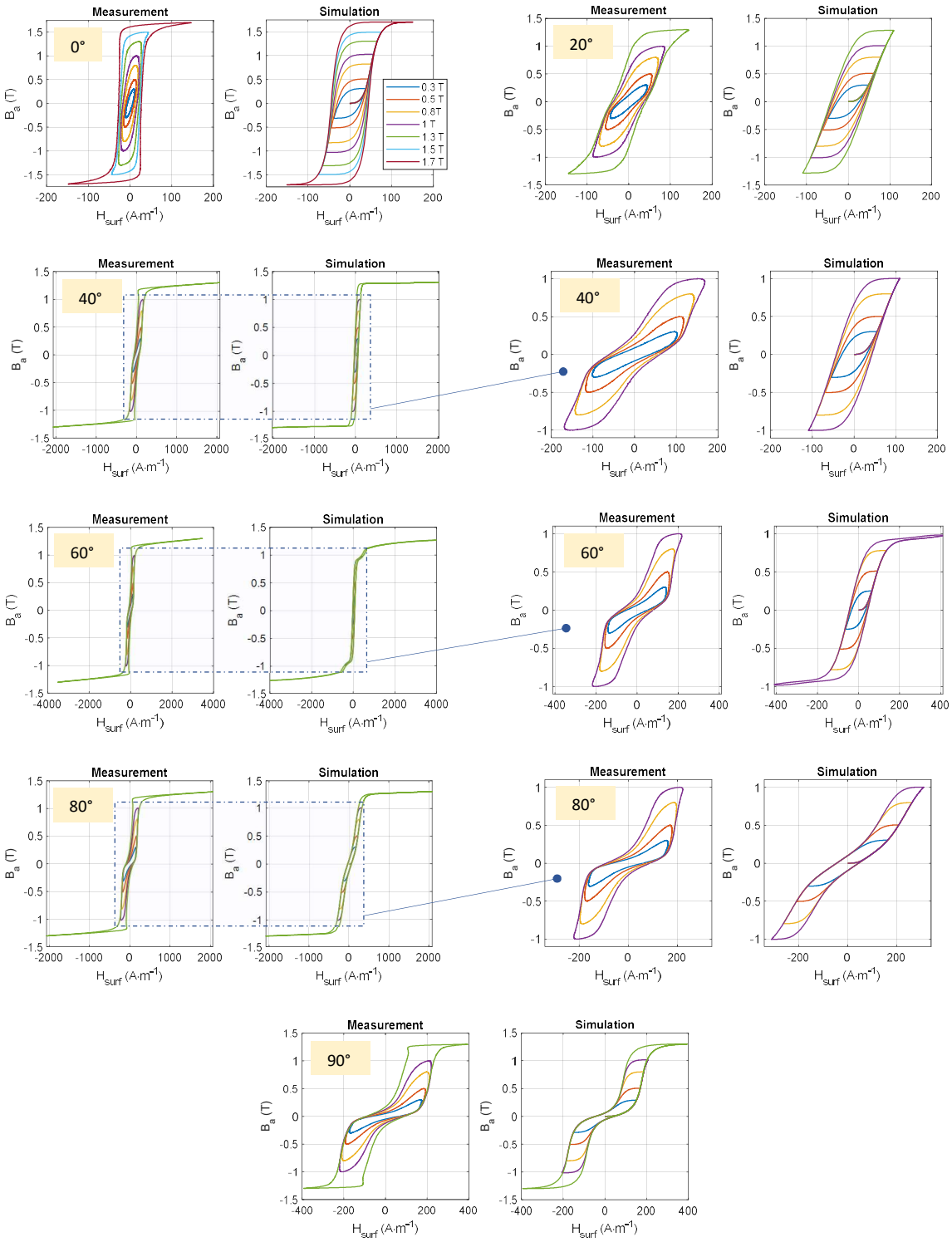

Fig. 7 Comparison simulation/measurement for quasi-static minor centered cycles under unidirectional alternating conditions and six different angles (optimized axis scale).

Fig. 8 gives an algorithm to summarize the MSM-DF model implementation, including step-by-step explanations.

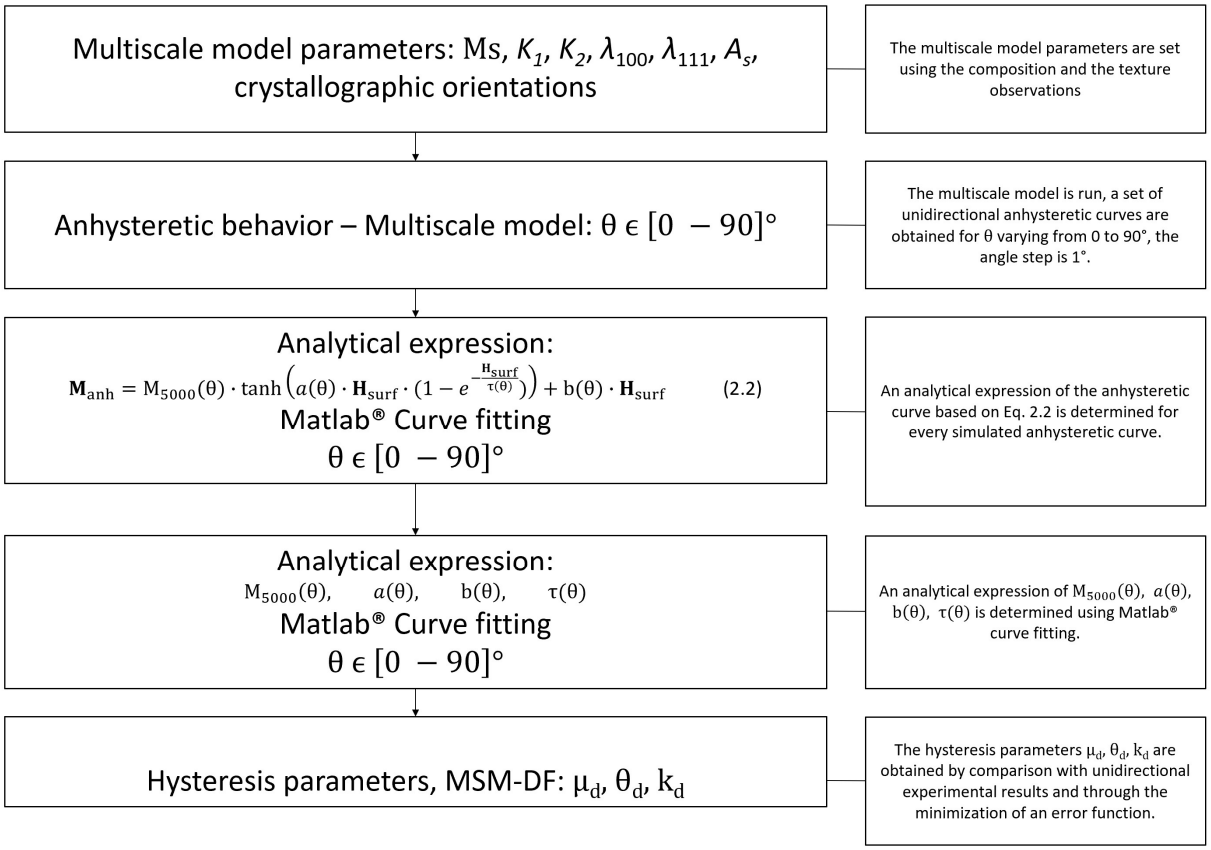

Fig. 8 – Algorithm for the MSM-DF model implementation.

3 – Comparison simulations/measurements under rotational magnetization

The importance of rotational magnetization behaviors in understanding the magnetization mechanisms was demonstrated a long time ago [1][2]. Still, characterization standards are in need, and getting reliable measurements is not an easy task. All the experimental results under rotational magnetization displayed in this manuscript have been measured with the same experimental setup (depicted in Fig. 9 below) [37][44].

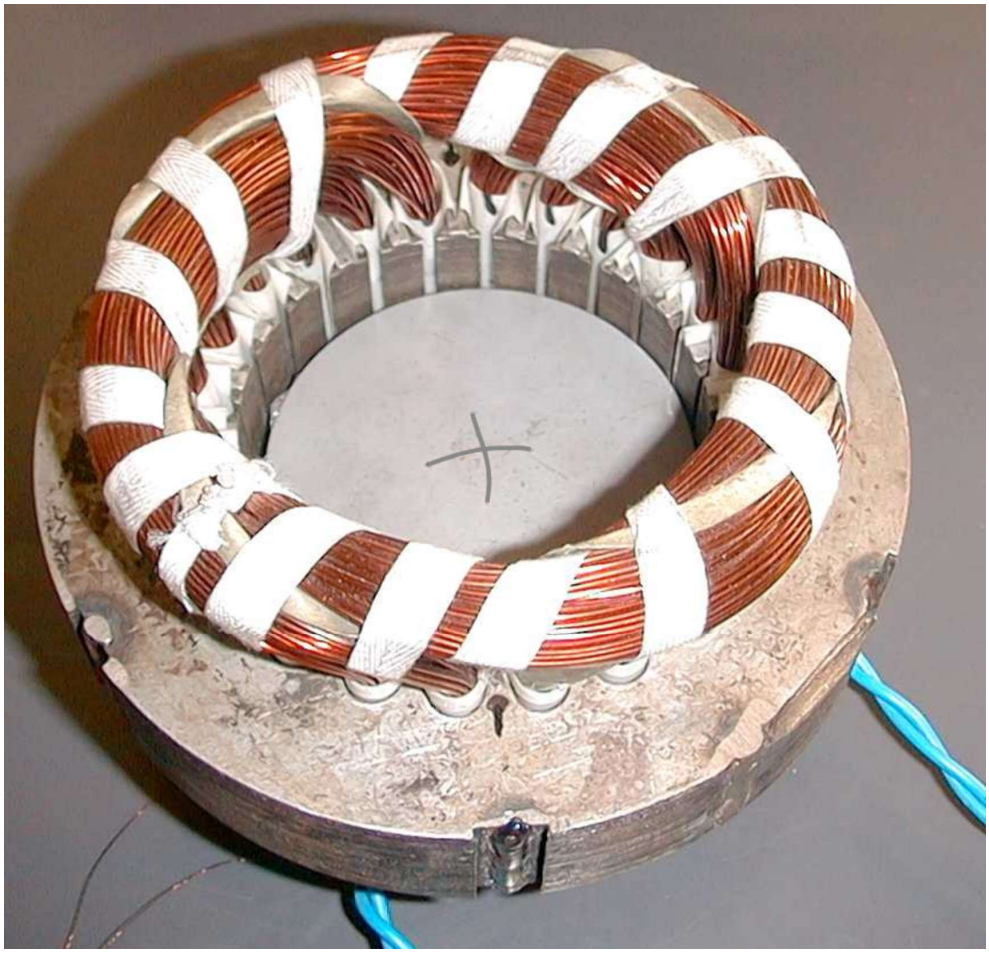

Fig. 9 Experimental setup picture.

A cylindrical magnetizing yoke was used. All the GO FeSi specimens tested were disks (80 mm diameter), their grade was M140-27. Two single turn local search coils, 20 mm wide each and positioned in quadrature in the center of the tested specimens, were used to measure $\mathbf{B}_a$. Similarly, two H-coils, also 20 mm wide and positioned tangent to the surface of the sample to be characterized, were used for $\mathbf{H}_{surf}$. All the tested specimens were placed in a way to align their RD with the system X-axis. A 2 mm gap between the specimen and the magnetizing yoke was set to ensure the magnetization homogeneity. Both $\mathbf{B}_a$ and $\mathbf{H}_{surf}$ imposed amplitude tests were done. Their consistencies were ensured through digital feedback. Characterizations were recorded in

clockwise and anticlockwise directions, and the final results average both directions and multiple periods. More details on the characterization setup can be found elsewhere [37][44]. Fig. 10 below gives comparisons of simulations and measurements for the loci curves (path drawn by the tip of $\mathbf{H}_{surf}$ and $\mathbf{B}_a$) under different imposed levels of $\mathbf{H}_{surf}$ circular magnetic field excitation (with the orthogonal components H_{surfx} and H_{surfy} sinusoidal and cosinusoidal, respectively). GO FeSi material is tested, and the simulation parameters are those of Tab. 1 (μ_d, θ_d), Tab. 2, and Tab. 3. Fig. 11 shows the simulated and measured associated hysteresis cycles, projections of $\mathbf{H}_{surf}$ and $\mathbf{B}_a$ on both the RD and TD axis.

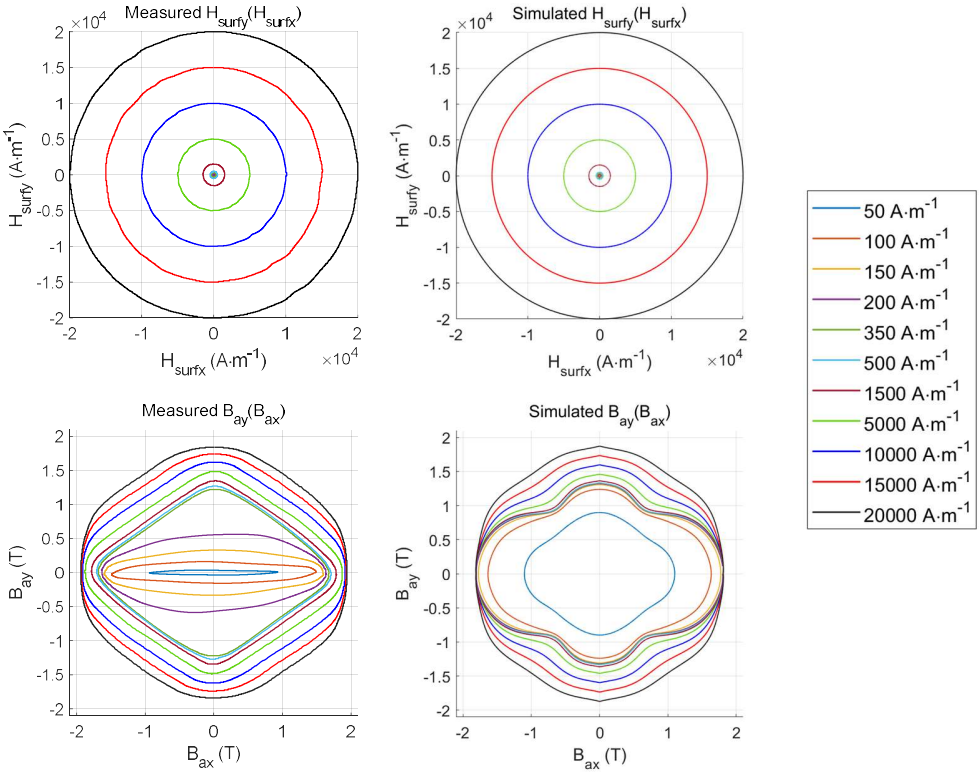

Fig. 10 $\mathbf{B}_a$ and $\mathbf{H}_{surf}$ loci curves, comparison simulations / measurements for different levels of imposed rotational $\mathbf{H}_{surf}$.

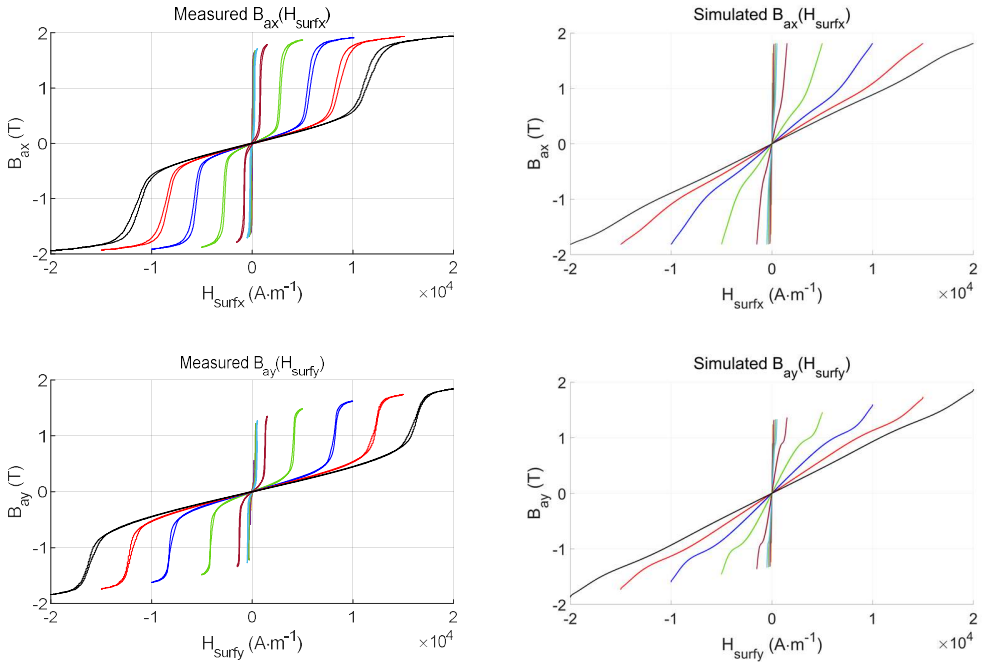

Fig. 11 Simulated and measured RD and TD hysteresis cycle for different levels of imposed rotational $\mathbf{H}_{surf}$. The colors of curves correspond to those from Fig. 8.

The observation of Fig. 10 and 11 leads to multiple conclusions. If the MSM-DF model fidelity is evident in the high induction level range, it is not below 350 A·m^{-1}. Numerous reasons can be found to justify those differences, including in the first place:

- divergences between the crystallographic and magnetoelastic properties of the specimens tested and used to set the simulation parameters. In the same electrical steel grade, significant differences in the magnetic response have already been noticed and discussed in the scientific literature (material processing, cutting, punching, etc., are the source of residual stresses variations changing the magnetic response drastically [17][45][46]). The saturation level is slightly lower in measurement, confirming divergences in some fundamental properties.
- Limitations of the simulation assumptions in the low induction range.
- Limitations of the experimental setup.

Even if RD exhibits softer magnetic properties in simulation and measurement, the supposedly unfavorable 55° direction is not evident in the experimental results (however, it is clearly distinguishable in the imposed $\mathbf{B}_a$ regime, as discussed below). It is also interesting to observe its progressive disappearance in both simulations and measurements for the high $\mathbf{H}_{surf}$ levels. This observation is justified by the predominance of W_α^H over the other energies.

In the following figures (Fig. 12, 13), the specimen is tested under circular $\mathbf{B}_a$ imposed conditions (orthogonal components B_{ax} and B_{ay} sine and cosine, respectively). The simulation results are obtained explicitly, using the $\mathbf{H}_{surf}$ imposed model. For each simulation step time t, a window of $\mathbf{H}_{surf}$ centered around its value at t = t – dt is tested (+/- ΔH, +/- Δθ). Where ΔH and Δθ are set depending on max($\mathbf{B}_a$) and dt.

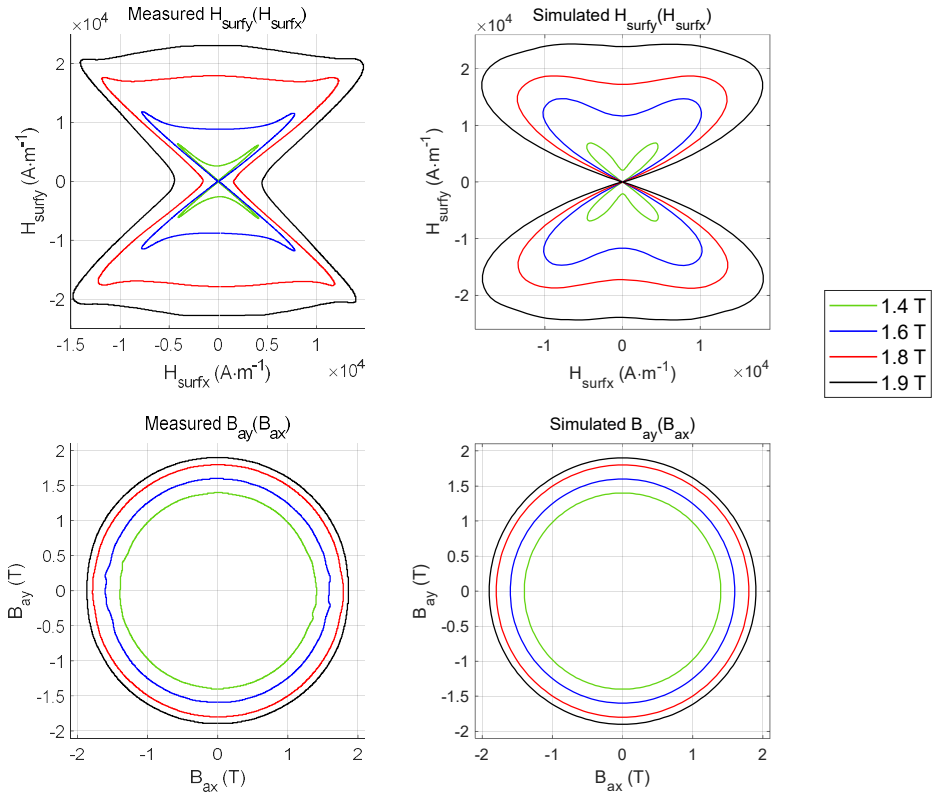

Fig. 12 $\mathbf{B}_a$ and $\mathbf{H}_{surf}$ loci curves, comparison simulations / measurements for 4 levels of imposed rotational $\mathbf{B}_a$.

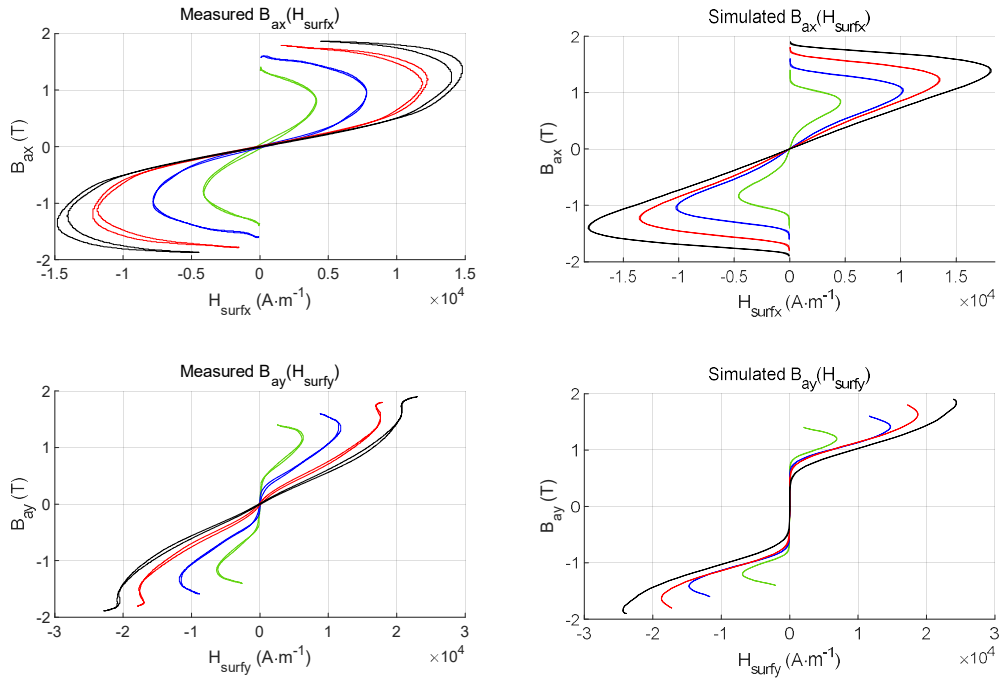

Fig. 13 Simulated and measured RD and TD hysteresis cycle for 4 levels of imposed rotational $\mathbf{B}_a$.

Just like the $\mathbf{H}_{surf}$ imposed curves, under imposed sinus, rotating $\mathbf{B}_a$, the trajectories of the simulation and the experimental results show close tendencies. The fit is not perfect (probably for the reasons listed hereinbefore), but the model well anticipates most of the peculiar and unusual ferromagnetic behaviors.

In Fig. 12, the magnetization level is limited to 1.9T. Similarly, Fig. 5 in Ito et al. [47] is limited to 1.7 T. The experimental results in Fig. 12 show that $\mathbf{H}_{surf}$ in the x-direction (RD) is getting higher when the magnetization levels increase. This effect is not visible in Fig. 12 simulation results nor in [47]. It is now evident in Fig. 14, where simulations have been conducted for much higher magnetization levels, $\mathbf{H}_{surf}$ starts increasing for magnetization levels higher than 2T.

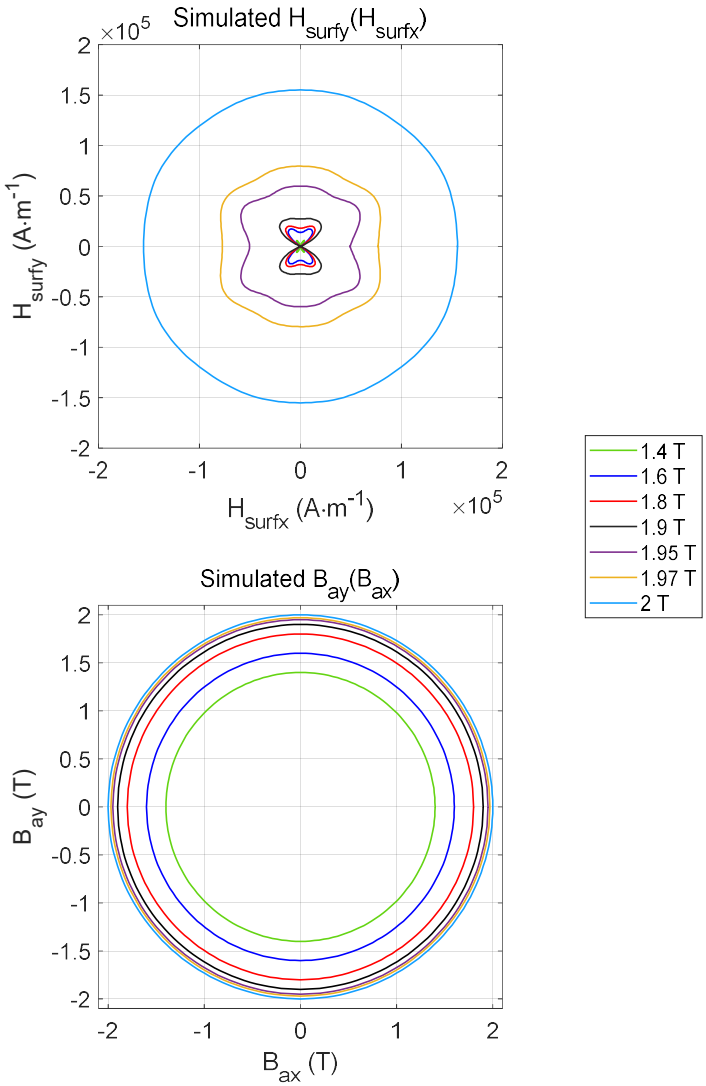

Fig. 14 $\mathbf{B}_a$ and $\mathbf{H}_{surf}$ loci curves, for 7 levels of imposed rotational $\mathbf{B}_a$.

M_s the saturation magnetization is constant. For a given direction, once M_s is reached, no further magnetization variations are possible so that the $\mathbf{H}_{surf}$ loci curve ends up in a quasi-perfect circle (Fig. 14).

It is essential to emphasize the predictive nature of the MSM-DF model, especially true under high magnetic field levels when the hysteresis loss is dropping. In such conditions, the MSM-DF relies mainly on the anhysteretic MSM contribution. It is worth mentioning that MSM is not a

fitting procedure. The model parameters are identified from a limited number of independent experiments, and the simulation results are compared to very different types of experiments.

It is also remarkable that although the hardest direction (55°) is undoubtedly present (Fig. 11 confirms this, especially for the green curves, just below the magnetization elbow), it is not evident when measuring under imposed rotational $\mathbf{H}_{surf}$, and the model correctly reflects that behavior. It is true that the data in Fig. 10 does not match precisely between simulation/measurement but the relative changes of the imposed rotational $\mathbf{B}_a$ butterfly are much smaller in Fig. 10 than the imposed rotational $\mathbf{H}_{surf}$ butterfly in Fig. 12.

A small hysteresis (difference between “ascending” and “descending” branches) can be observed in the experimental $H_{surfx}(B_{ax})$ and $H_{surfy}(B_{ay})$ cycles Fig. 12. The total rotational loss can be split into the P_x and P_y components which are proportional to the area of the corresponding B-H loops. However, especially at higher excitation, it is possible that the experimental B-H loop (as shown in Fig. 13) can have local “negative” areas, due to the phase differences between the sensors resulting from their angular misalignment. This is one of the reasons why the value of power loss has to be averaged from clockwise and anticlockwise measurements. Investigation of this experimental phenomenon is beyond the scope of this paper, but extensive studies were already published elsewhere [37][44].

4 – Conclusions and perspectives

A vector anisotropic hysteresis model (MSM-DF) has been described in this manuscript. It is based on the combination of a multiscale model for the simulation of the anhysteretic magnetization and a hysteresis contribution relying on an analogy between ferromagnetic

domain wall motions and mechanical dry-frictions. The model is validated by comparing simulation and experimental results obtained in the lamination plane of a GO FeSi electrical steel and circular magnetic field excitation ($\mathbf{B}_a$ or $\mathbf{H}_{surf}$ imposed). The model succeeds in the restitution and prediction of multiple peculiar behaviors, including the loci curves' butterfly shape under rotational sinus $\mathbf{B}_a$ and sinus $\mathbf{H}_{surf}$ imposed conditions (especially true at high magnetic field).

The remarkably different influence of the unfavorable 55° direction under rotational circular $\mathbf{B}_a$ and circular $\mathbf{H}_{surf}$ imposed conditions is also qualitatively well anticipated by the model. It reveals the fidelity with the magnetic structure of the model under completely different magnetization regimes.

Under high-level, low-frequency circular magnetization where hysteresis effects are disappearing, magnetization processes rely mostly on the anhysteretic contribution. The MSM-DF model then reduces to the MSM and consequently becomes more predictive [27][39][48].

This behavior opens exciting perspectives in the domain of magnetic NDT [49][50]. Such experimental conditions could be used to isolate the anhysteretic contribution. The combination of experimental results and the MSM-DF model could also define an elegant way to anticipate residual mechanical stresses in ferromagnetic materials.

References

[1] A.J. Moses, “Importance of rotational losses in rotating machines and transformers,” *J. of Mat. Eng. And Perf. 1*, pp. 235 – 244, 1992.

[2] A. Moses, B. Thomas, “Problems in the design of power transformers,” *IEEE Trans. Mag.*, vol. 10, n° 2, pp. 148 – 150, 1974.

[3] D. Binesti, J.P. Ducreux, “Core losses and efficiency of electrical motors using new magnetic materials,” *IEEE Trans. Mag.*, vol. 32, n° 5, pp. 4887 – 4889, 1996.

[4] D. Jiles, “Introduction to magnetism and magnetic materials,” (Third ed.), CRC Press, Florida, USA, 2015.

[5] G. Bertotti, “Hysteresis in magnetism,” Academic Press, Boston, 1998.

[6] M.A. Raulet, B. Ducharne, J.P. Masson, G. Bayada, “The magnetic field diffusion equation including dynamic hysteresis: a linear formulation of the problem,” *IEEE Trans. Mag.*, vol. 40, n° 2, pp. 872 – 875, 2004.

[7] E. Dlala, “Comparison of models for estimating magnetic core losses in electrical machines using the finite-element methods,” *IEEE Trans. Mag.*, vol. 45, n° 2, pp. 716 – 725, 2009.

[8] K. Komeza, M. Dems, “Finite-element and analytical calculations of no-load core losses in energy-saving induction motors,” *IEEE Trans. Ind. Elect.*, vol. 59, n° 7, pp. 2934 – 2946, 2012.

[9] S.E. Zirka, Y.I. Moroz, C.M. Arturi, “Accounting for the influence of the tank walls in the zero-sequence topological model of a three-phase, three-limb transformers,” *IEEE Trans. Pow. Del.*, vol. 29, n° 5, pp. 2172 – 2179, 2014.

[10] S. Somkun, A. J. Moses, P. I. Anderson and P. Klimczyk, "Magnetostriction Anisotropy and Rotational Magnetostriction of a Nonoriented Electrical Steel," *IEEE Trans. Mag.*, vol. 46, n° 2, pp. 302-305, 2010.

[11] Y. He, M. Mehdi, E.J. Hilinski, A. Edrisy, “Through-process characterization of local anisotropy of Non-oriented electrical steel using magnetic Barkhausen noise,” *J. Magn. Magn. Mater.,* vol. 453, pp. 149-162, 2018.

[12] B. Fryskowski, “Experimental evaluation of magnetic anisotropy in electrical steel sheets,” *J. Magn. Magn. Mater.,* vol. 320, Iss. 3-4, pp. 515-522, 2008.

[13] K. Chwastek, “Anisotropic properties of non-oriented steel sheets,” *IET Elect. Power Appl.*, vol. 7, n° 7, pp. 575-579, 2013.

[14] N. Leuning, S. Steentjes, M. Heller, S. Korte-Kerzel, K. Hameyer, “On the correlation of crystallographic macro-texture and magnetic magnetization anisotropy in non-oriented electrical steel,” *J. Magn. Magn. Mater.,* vol. 490, 2019.

[15] F.J.G Landgraf, T Yonamine, M Emura, M.A Cunha, “Modelling the angular dependence of magnetic properties of a fully processed non-oriented electrical steel,” *J. Magn. Magn. Mater.,* vol. 254-255, pp. 328 – 330, 2003.

[16] F. Jiang, M. Rossi, and G. Parent, “Anisotropy model for modern grain oriented electrical steel based on orientation distribution function,” *AIP Adv. 8*, 056104, 2018.

[17] A. Belahcen, D. Singh, P. Rasilo, F. Martin, S. G. Ghalamestani and L. Vandevelde, "Anisotropic and Strain-Dependent Model of Magnetostriction in Electrical Steel Sheets," *IEEE Trans. Mag.*, vol. 51, n° 3, pp. 1 - 4, 2015.

[18] C. Appino, C. Ragusa, F. Fiorillo, “Can rotational magnetization be theoretically assessed?,” *Int. J. of App. Electromag. and Mech.*, vol. 44, n° 3-4, pp. 355 – 370, 2014.

[19] I.D. Mayergoyz, “Mathematical models of hysteresis,” *IEEE Trans. Mag.*, vol. 22, iss. 5, pp. 603 – 608, 1986.

[20] I.D. Mayergoyz, G. Friedman, “Isotropic vector Preisach model of hysteresis,” *J. App. Phys.*, vol. 61, pp. 2022 – 2023, 1987.

[21] E.D. Torre, E. Pinzaglia, E. Cardelli, “Vector modeling Part I: Generalized hysteresis model,” *Phys. B* 372, pp. 111 – 114, 2006.

[22] M. d’Aquino, C. Serpico, C. Visone, A.A. Adly, “A new vector model of magnetic hysteresis based on a novel class of play hysterons,” *IEEE Trans. on Mag.*, vol. 39, n° 5, pp. 2537 – 2539, 2003.

[23] A.J. Bergqvist, “A simple vector generalization of the Jiles-Atherton model of hysteresis,” *IEEE Trans. on Mag.*, vol. 32, n° 5, pp. 4213 – 4215, 1996.

[24] J.V. Leite, N. Sadowski, P. Kuo-Peng, N.J. Batistela, J.P.A. Bastos, A.A. De Espindola, “Inverse Jiles-Atherton vector hysteresis model”, *IEEE Trans. Mag.*, vol. 40, n°4, pp. 1769 – 1775, 2004

[25] B. Upadhaya, P. Rasilo, L. Perkkiö, P. Handgruber, A. Benabou, A. Belahcen, A. Arkkio, “Alternating and rotational loss prediction accuracy of vector Jiles-Atherton model,” *J. Magn. Magn. Mater.,* vol. 527, 167690, 2021.

[26] A. Bergqvist, “Magnetic vector hysteresis model with dry friction-like pinning,” *Physica B: Cond. Matter*, vol. 233, Issue 4, pp. 342 – 347, 1997.

[27] O. Hubert, L. Daniel, “Multiscale modeling of the magneto-mechanical behavior of grain-oriented silicon steels,” *J. Magn. Magn. Mater.,* vol. 320, pp. 1412 – 1422, 2008.

[28] N.S. Podolefsky, N.D. Finkelstein, “Use of analogy in learning physics: the role of representations,” *Phys. Rev. ST Phys. Educ. Res.*, vol. 2, iss. 2, pp. 020101-1 - 020101-10, 2006.

[29] J. Wojewoda, A. Stefanski, M. Wiercigroch, T. Kapitaniak, “Hysteretic effects of dry friction: modelling and experimental studies,” *Phil. Trans. R. Soc. A.*, vol. 366, pp. 747 – 765, 2007.

[30] C. Cardi, P. Nozières, “Hysteresis and elastic interactions of microasperities in dry friction,” *Eur. Phys. J. B*, vol. 4, pp. 233 – 246, 1998.

[31] A.K. Padthe, B. Drincic, J. Oh, D.D. Rizos, S.D. Fassois, D.S. Bernstein, “Duhem modeling friction-induced hysteresis,” IEEE Cont. Syst. Mag., vol. 28, n° 5, pp. 90 – 107, 2008.

[32] V. Lampaert, J. Swevers, “Online identification of hysteresis functions with non-local memory,” 2001 IEEE/ASME Int. Conf. on Adv. Int. Mech. Proceedings (Cat. N°01TH8556), vol. 2, pp. 833 – 837, 2001.

[33] F. Henrotte, K. Hameyer, “A dynamical vector hysteresis model based on an energy approach,” *IEEE Trans. Magn.*, vol. 42, n° 4, pp. 899 – 902, 2006.

[34] W. Baltensperger, J. S. Helman, “Dry friction in micromagnetics,” *IEEE Trans. Magn.*, vol. 42, n° 4, pp. 899 – 902, 2006.

[35] B. Ducharne, D. Guyomar, G. Sebald, “Low frequency modelling of hysteresis behaviour and dielectric permittivity in ferroelectric ceramics under electric field,” *J. Phys. D: Appl. Phys.*, vol. 40, pp. 551 – 555, 2007.

[36] D. Guyomar, B. Ducharne, G. Sebald, D. Audigier, “Fractional derivative operators for modeling the dynamic polarization behavior as a function of frequency and electric field amplitude,” *IEEE Trans. on Ultras. and Freq. Cont.*, vol. 56, n°3, pp. 437 – 443, 2009.

[37] S. Zurek, “Characterisation of Soft Magnetic Materials Under Rotational Magnetisation”, Boca Raton, FL, USA:CRC Press, 2018.

[38] L. Daniel, O. Hubert, N. Buiron, R. Billardon, “Reversible magneto-elastic behavior: a multiscale approach,” *J. Mech. Phys. Solids,* vol. 56, pp. 1018 – 1042, 2008.

[39] L. Daniel, M. Rekik, O. Hubert, “A multiscale model for magneto-elastic behaviour including hysteresis effects,” *Arch. Appl. Mech.,* vol. 84, iss. 9, pp. 1307 – 1323, 2014.

[40] F. Fiorillo, L.R. Dupre, C. Appino, A.M. Rietto, “Comprehensive model of magnetization curve, hysteresis loops, and losses in any direction in grain-oriented Fe-Si,” *IEEE Trans. Magn.*, vol. 38, n° 3, pp. 1467 – 1476, 2002.

[41] A.P.S. Baghel, B. Sai Ram, K. Chwastek, L. Daniel, S.V. Kulkarni, “Hysteresis modelling of GO laminations for arbitrary in-plane directions taking into account the dynamics of orthogonal domain walls,” *J. Magn. Magn. Mater.,* vol. 418, pp. 14 – 20, 2016.

[42] S. Zurek, R. Rygal, “Asymmetry of magnetic properties of grain-oriented electrical steel,” *Przeglad Elektrotechniczny*, 2009.

[43] F. Fiorillo, L. Dupré, “Comprehensive model of magnetization curve, hysteresis loops, and losses in any direction in Grain-Oriented Fe-Si,” *IEEE Trans. Mag.*, vol. 38, n° 3, pp. 1467 – 1476, 2002.

[44] S. Zurek, T. Meydan, Rotational power losses and vector loci under controlled high flux density and magnetic field in electrical steel sheets, IEEE Transactions on Magnetics, Vol. 42, No 10, 2006, p. 2815 – 2817.

[45] H. Naumoski, B. Riedmüller, A. Minkow, U. Herr, "Investigation of the influence of different cutting procedures on the global and local magnetic properties of non-oriented electrical steel," *J. Magn. Magn. Mater.,* vol. 392, pp. 126 – 133, 2015.

[46] H.A. Weiss, P. Tröber, R. Golle, S. Steentjes, N. Leuning, S. Elfgen, K. Hameyer, W. volk, "Impact of punching parameter variations on magnetic properties of nongrain-oriented electrical steel," *IEEE Trans. on Ind. App.*, vol. 54, n°6, pp. 5869 – 5878, 2018.

[47] S. Ito, T. Mifune, T. Matsuo, C. Kaido, "Energy-Based Magnetization and Magnetostriction Modeling of Grain-Oriented Silicon Steel Under Vectorial Excitations," *IEEE Trans. Mag.*, vol. 52, n° 5, pp. 1 – 4, 2016.

[48] M. Rekik, L. Daniel, O. Hubert, "Equivalent stress model for magnetic hysteresis losses under biaxial loading," *IEEE Trans. Mag.*, vol. 50, n° 4, 2001604, 2014.

[49] B. Gupta, B. Ducharne, T. Uchimoto, G. Sebald, T. Miyazaki, T. Takagi, "Comparison of electromagnetic nondestructive testing of creep-degraded high-chromium ferritic steels," *NDT & E. Int.*, vol. 118, 102399, 2021.

[50] B. Ducharne, B. Gupta, Y. Hebrard, J. B. Coudert, "Phenomenological model of Barkhausen noise under mechanical and magnetic excitations," *IEEE Trans. Mag.*, vol. 99, pp. 1-6, 2018.